



Analysing the Probability of Detection of Shallow Spherical Defects by Means of Pulsed Thermography

E D.'Accardi¹ · D Palumbo¹ · V Errico¹ · A Fusco¹ · A Angelastro¹ · U Galietti¹

Received: 18 October 2022 / Accepted: 13 February 2023 / Published online: 11 March 2023
© The Author(s) 2023

Abstract

The capability of Active Thermography (AT) techniques in detecting shallow defects has been proved by many works in the last years, both on metals and composites. However, there are few works in which these techniques have been used adopting simulated defects more representative of the real ones. The aim of this work is to investigate the capability of Pulsed Thermography of detecting shallow spherical defects in metal specimens produced with laser powder bed fusion (L-PBF) process and characterized by a thermal behaviour very far from the flat bottom hole and so near to the real one. In particular, the quantitative characterization of defects has been carried out to obtain the Probability of Detection (PoD) curves. In fact, it is very common in non-destructive controls to define the limits of defect detectability by referring to PoD curves based on the analysis of flat bottom holes with a more generous estimation and therefore not true to real defect conditions. For this purpose, a series of specimens, made by means of Laser-Powder Bed Fusion technology (L-PBF) in AISI 316L, were inspected using Pulsed Thermography (PT), adopting two flash lamps and a cooled infrared sensor. To improve the quality of the raw thermal data, different post-processing algorithms were adopted. The results provide indications about the advantages and limitations of Active Thermography (AT) for the non-destructive offline controls of the structural integrity of metallic components.

Keywords Pulsed thermography (PT) · Non-destructive techniques (NDT) · Probability of detection (PoD) · Laser-powder bed fusion (L-PBF) · Additive Manufacturing (AM)

1 Introduction

Active infrared thermography has been usually applied as a non-destructive technique in many industrial applications and fields, to detect and characterize shallow defects, from composite [1–5] to metals [3, 6–8].

The main advantages of the use of active thermographic techniques are known [1]. In particular, these techniques allow for a full-field non-destructive control, without the need for direct contact with the component, they are very fast and require an external heat source to stimulate the component for a few seconds. For high diffusivity materials like metals, due to the high heat diffusive phenomena, the use of active thermographic techniques can be considered only for surface or subsurface controls [7]. Basically, pulsed thermography and lock in thermography are commonly used among optical infrared thermography approaches, that includes also

the use of other techniques, such as induction thermography, pulse compression thermography, and laser spot thermography [9–21].

In Pulsed Thermography (PT), the investigated material is stimulated by a short-duration energy pulse (likely, flash lamp, eddy-current, laser, etc.), and the thermal sequence is collected by an infrared sensor. The raw thermal data are then processed by applying post-processing algorithms (i.e. Pulsed Phase Thermography (PPT), Thermographic Signal Reconstruction (TSR), Principal Component Thermography (PCT), etc.) [15–18].

Like all non-destructive techniques, also Pulsed Thermography (PT) requires experimental tests in which the test and analysis parameters must be set. This “calibration” approach needs the extensive use of specimens made of the same material and with simulated defects as similar as possible to the real defects [7, 8]. However, it is not easy to simulate real flaws because of difficulties in master sample production and related high costs. Therefore, most of the literature works concerns the analysis of Flat Bottom Holes (FBHs), which

✉ E D.'Accardi
ester.daccardi@poliba.it

¹ Politecnico di Bari, Via Edoardo Orabona 4, 70125 Bari, Italy

can only very remotely simulate the thermal behaviour of a real defect and so can not useful to characterize the same [7].

The aim of this work is to investigate the capability of Active Thermography in detecting shallow spherical defects in metal specimens produced with the Laser-Powder Bed Fusion (L-PBF) process. The spherical defects simulate better, with respect to the FBHs, the thermal behaviour of real defects as these latter are characterized by a low value of the reflection coefficient. In particular, the quantitative characterization of defects has been carried out to obtain the Probability of Detection (PoD) curves [21–23].

Generally, for a quantitative non-destructive technique or method, the Probability of Detection (PoD) is a metric to describe the accuracy of a test. This statistical method identifies in a quantitative way, how well a non-destructive inspection can detect and characterize defects. This methodology allows for a simple comparison also among the application of different non-destructive techniques. Up to now, there have been several studies concerning the determination of the PoD of standard and more conventional non-destructive methods like ultrasonics, eddy current, and radiography [24, 25]. Some works also regard the application of active thermography with this purpose, in particular, lock-in and pulsed techniques, but considering in most cases FBHs defects [2–3]. In order to determine the PoD curve, a relationship between the variable that describes the defect and the one that characterizes the signal contrast is necessary [2, 3, 21–23].

In this work, to obtain the PoD curves, a series of specimens in AISI 316L, for a total of twelve, were produced by means of L-PBF technology. A series of defects of hollow spherical shape, known size and at different depths, were created within the specimens. Defects were produced layer-by-layer by not scanning the powder in the defect area with the laser beam. Moreover, given the layer-by-layer construction method of the L-PBF process, the defects themselves presented unmelted powder trapped within them. In this way, it is possible to evaluate the capability of Pulsed Thermography in detecting shallow defects, more “close” to the real defects that are present in metallic components, as in casting.

Several thermographic tests have been carried out using the pulsed thermography technique in reflection configuration, with two flash lamps and a cooled sensor. Different post-processing algorithms were considered to improve the quality of the raw thermal data in terms of signal-to-noise ratio (SNR), and, in particular, Pulsed Phase Thermography (PPT) [1, 6, 7, 15], Thermographic Signal Reconstruction (TSR) [16, 17], Principal Component Thermography (PCT) [18], Slope and R^2 [19].

In addition, the PoD curves were compared to analyse the performance of the technique and establish, in a quantitative way, the limits of the used setup, parameters, and post-processing algorithms to detect spherical defects.

2 Theoretical Background: Pulsed Thermography and Post-processing Algorithms

The concept of Pulsed Thermography (PT) as a non-destructive technique for high diffusivity material inspection consists of applying in a very short time a powerful energy pulse to the specimen under investigation and then recording the temperature decay [1]. According to the thermal diffusion phenomena, the presence of a defect interferes with the diffusion of the heat and appears as an area with a different temperature than its surroundings. The specimen surface is heated by a Dirac-shaped flash excitation with an energy density of Q . Under the hypothesis of a one-dimensional heat transfer in-depth direction, semi-infinite plate and neglecting the heat losses due to radiation and convection, the temperature T of the surface $z = 0$ above a defect at a depth d , can be described as follows [26]:

$$T(0, t) = \frac{Q}{\sqrt{\pi\rho c k i}} \left[1 + 2 \sum_{n=1}^{\infty} \gamma^n \exp\left(-\frac{n^2 d^2}{\alpha t}\right) \right] \quad (1)$$

where ρ is the density, c is the specific heat capacity, k is the thermal conductivity, α is the thermal diffusivity of the material, and t represents the time. The coefficient γ describes the contrast of the thermal effusivities at the interface of the sound material to defect, which is very close to 1 only in the theoretical case of perfect reflection and a large discontinuity [7, 26, 27].

During the last years in which the pulsed thermography technique has been used for several applications, several post-processing algorithms were considered and adopted to improve the quality of the raw thermal data and then the signal-to-noise ratio such as Pulsed Phase Thermography (PPT) [1, 6, 7, 15], Thermographic Signal Reconstruction (TSR) [16, 17], Principal Component Thermography (PCT) [18], Slope and R^2 [19]. The theoretical background of each of these algorithms is well known, as reported in the mentioned works.

3 Probability of Detection (PoD)

The PoD is a quantitative measure of the capability of a non-destructive technique or methodology and allows the determination of the defect detection probability as a function of a parameter describing the defect geometry (ASME 3023–15) [2, 3, 21–23].

This methodology should produce output that can be summarized within a representative quantitative signal, ‘ \hat{a} ’, or a binary response, hit/miss. For this reason, starting signals will need some pre-processing to provide either ‘ \hat{a} ’ or hit/miss and

a parameter ‘ a ’ able to characterize the system, as inputs to these analysis methods.

In the case of PoD analysis of continuous response data, the methodology relies on Generalized Linear Models, where, simply, a defect parameter ‘ a ’ is required, which depends linearly on the measured signal ‘ \hat{a} ’. Generally, supposing that ‘ $g_a(\hat{a})$ ’ indicates the probability density function of the ‘ \hat{a} ’ related to a generic defect characteristic ‘ a ’, the PoD can be written as:

$$PoD(a) = \int_{\hat{a}_{dec}}^{\infty} g_a(\hat{a})d\hat{a} \tag{2}$$

With the hypothesis of a linear relation ‘ \hat{a} vs a ’ with normally distributed deviations, it is possible to write:

$$\hat{a}(a) = B_0 + B_1xa + \varepsilon \tag{3}$$

where ε is the measurement error, which usually follows the normal distribution with zero mean value μ and standard deviation σ_ε and, obviously, B_0 and B_1 are the coefficients of the linear regression. Normally, an analysis of source data ‘ \hat{a} vs. a ’ is implemented to choose the best model that can be described properly by a straight line with a good square correlation coefficient (R^2) and constant variance. This research includes the analysis of four models: ‘ \hat{a} vs. a ’, ‘ \hat{a} vs. $\log(a)$ ’, ‘ $\log(\hat{a})$ vs. a ’, and ‘ $\log(\hat{a})$ vs. $\log(a)$ ’.

After the choice of the best linear model, the PoD can be calculated by the relationship:

$$PoD = \Phi\left(\frac{a-\mu}{\sigma}\right) = \frac{1}{2}\left[1 + erf\left(\frac{a-\mu}{\sigma\sqrt{2}}\right)\right] \tag{4}$$

Equation 4 represents the expression of a cumulative normal distribution function, where erf is the error function and the parameters μ and σ are expressed as reported below as a function of the threshold ‘ th ’ above of which a defect can be detected:

$$\mu = \frac{\hat{a}_{th}-B_0}{B_1} \quad \sigma = \frac{\sigma_\varepsilon}{B_1}x\hat{a}_{th} \tag{5}$$

Usually, the values of B_0 , B_1 , σ_ε can be estimated by using the maximum-likelihood estimation method to achieve the best fitting of the analysed data set.

In non-destructive investigations that use this methodology to quantify defect reliability, the *Signal-to-Noise ratio (SNR)* or, equivalently, the *Normalized Contrast (CNR)*, or the simple contrast, of the temperature difference between defect and sound regions related to a generic thermogram or an analogs contrast measurement related to a post-processing thermal feature are used as variable \hat{a} . Instead, a parameter that describes the defect geometry needs to be found and usually, this parameter can be any mathematical representation



Fig. 1 Part of specimens manufactured for the thermographic analyses performed

of one or more defect characteristics, e.g. the diameter D , the depth d , the nominal area A and the aspect ratio D/d .

The hit/miss or 0/1 response, where one denotes the detected defect and zero denotes the undetectable defect, is made by the operator and depends on the threshold value and the region of interest (ROI) that define the defect and related sound zone [2, 3]. If the contrast related to a particular thermal feature is over the given value that is determined by the inspector, the hit source data is set equal to 1, instead, the miss data is obtained as 0. With the same logic of PoD analysis related to continuous phase response data, the first step for POD analysis of hit/miss response data is model identification. There are four models corresponding to four different link functions: logit, logistic or log-odds function, the probit or inverse normal function, the complementary log–log function, often called Weibull by engineers, and the loglog function. Both the log-normal and log-odds link functions are more often used to link binary data to defect characteristic ‘ a ’. The obtained results in terms of PoD curves can be considered practically equivalent in many cases [2]. Due to a number of available defects and obtained results in terms of linearity, in this study a hit/miss approach has been adopted, and the log-odds function has been used, as suggested in [2, 3].

4 Materials and Methods

4.1 Setup and Materials for the L-PBF Process and Experimental Plan

A series of specimens were fabricated with Laser-Powder Bed Fusion (L-PBF) technology, using the M1 Cusing commercial machine owned by Concept Laser (GE). Figure 1 shows a part of the printed specimens. The M1 machine was equipped with an Nd-YAG (Neodymium-doped Yttrium

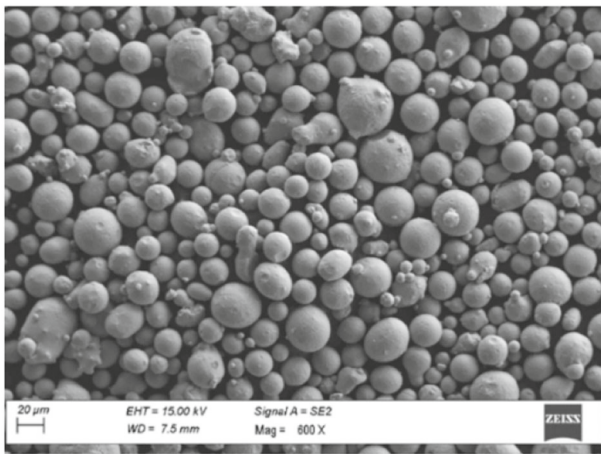


Fig. 2 Scanning Electron Micrographs (SEM) of the AISI 316L gas atomized powder

Aluminium Garnet) laser source having a wavelength of 1064 nm, a maximum laser power output in continuous mode of 100 W, and a beam spot diameter of 200 μm . The laser beam was guided through a mirror galvanometer on the powder bed, selectively drawing each layer to be produced. Figure 2 shows the metallic powder used for the fabrication of the specimens, which were subsequently analyzed by thermography. The material used was the AISI 316L, the particle size of the powder was in the range of 15–53 μm and its shape was spherical. This gas atomized powder was produced by Cogne Acciai Speciali S.p.a. (Italy) and its chemical composition, as certified by the manufacturer, is given in Table 1.

Hollow spheres of known size were created within the fabricated specimens to simulate the presence of defects. These defects, due to the construction method of the L-PBF process, are filled with unmolten powder, as can be seen in Fig. 3.

The specimens were fabricated using the process parameters shown in Table 2. The latter resulted from optimization conducted in previous works [28, 29]. An important expedient adopted in the arrangement of the specimen to be manufactured was a rotation of 45°, on the construction platform, with respect to the coating blade (see Fig. 4): this solution prevented the edges of the specimens were parallel to the coater, creating an uneven distribution or a barrier for the recoating of the powder. Furthermore, the specimens were manufactured using the random island strategy; each island had a size of 5 × 5 mm². The islands were scanned by the laser randomly on each layer and this was useful to reduce

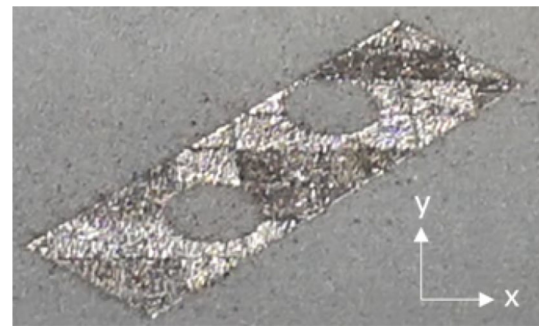


Fig. 3 The unmolten powder inside the defects as it appears during fabrication

Table 2 Process parameters used to produce the specimens

Process parameters	Values
Laser power (W)	100
Scanning speed (mm s ⁻¹)	200
Laser spot diameter (μm)	200
Hatch distance (μm)	140
Layer thickness (μm)	30

the residual thermal stresses [30, 31]. However, as the specimen grew in a layer-by-layer manner in the Z direction, there was a 1 mm translation, in X and Y directions, of the islands of a layer with respect to those of the previous layer: this solution prevented the porosities formation between layers (see Fig. 4).

Defects were created within each specimen with the distribution in space shown in Fig. 5 and described in detail in Table 3.

The aspect ratio D/d has been chosen considering the theoretical limit of 2–3 found in the literature for flat bottom holes. Of course, the limit can be assumed to be certainly more severe in the case of spherical defects. As already underlined in previous sections, the AM process allowed us to design the sample/master specimens with the desired aspect ratios. The possibility to produce master specimens made of metallic materials is fundamental for calibrating the technique and then applying the same in real industrial applications on metallic components.

Figure 6 shows the cross-section of specimen 2 (spheres with a diameter of 6 mm) and confirms the correct shape, sizes, and position of defects within the specimens.

Table 1 Chemical composition (wt%) of the AISI 316L gas atomized powders used to make the specimens

Element	Cr	Ni	Mo	Mn	Si	Cu	C	S	N	P	O	Fe
wt%	16.0–18.0	11.0–13.0	2.0–3.0	2.0	0.75	0.50	0.03	0.010	0.10	0.025	0.10	Bal

Fig. 4 Schematic representation of the island shifts in the different layers: **a** layer 1; **b** layer 2; **c** layer 3

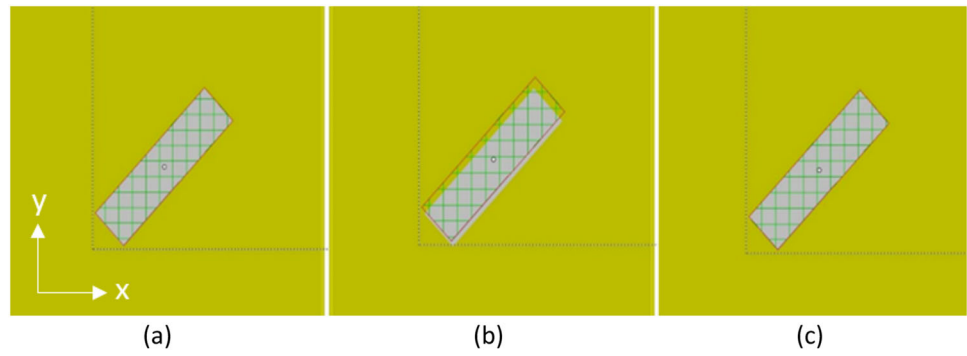


Fig. 5 a Defect and specimen geometry reported as an example for specimen 1 and **b** schematic view of the defect distribution within the manufactured specimens

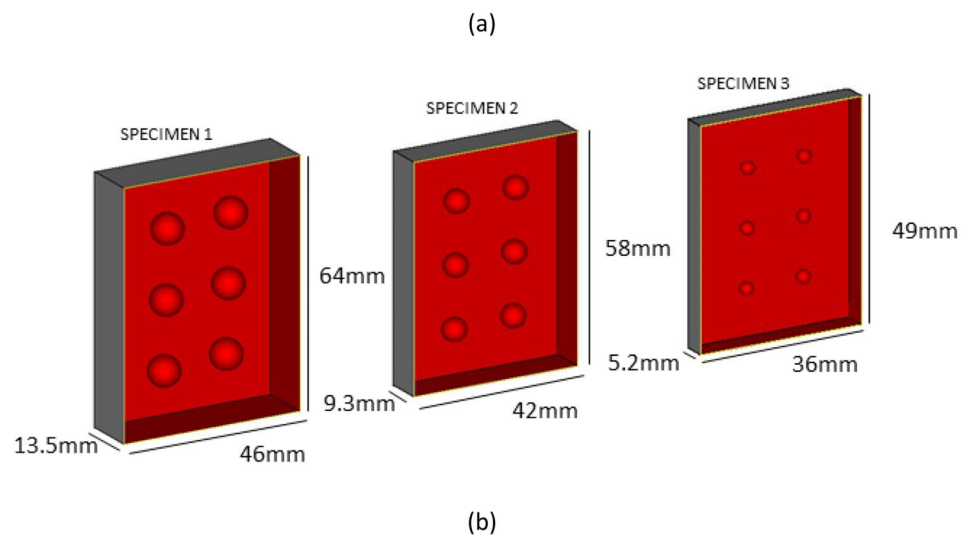
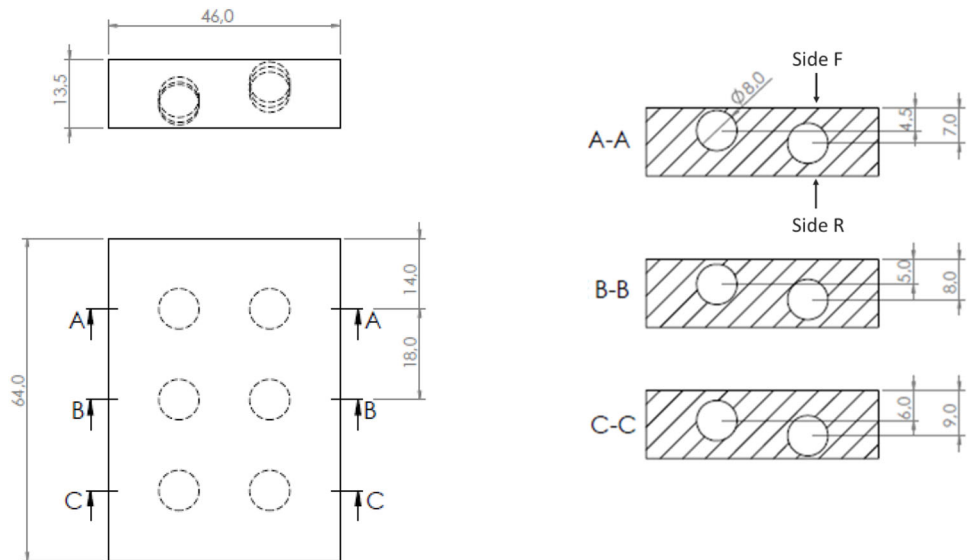


Table 3 Full experimental plan of induced spherical defects. D is the diameter of the sphere, d represents the distance between the beginning of the sphere and the external face of the specimen

Specimen 1 × 4 Diameter (D) 8.00 [mm]		Specimen 2 × 4 Diameter (D) 6.00 [mm]		Specimen 3 × 4 Diameter (D) 3.00 [mm]	
Depth (d) [mm]	Aspect ratio (D/d)	Depth (d) [mm]	Aspect ratio (D/d)	Depth (d) [mm]	Aspect ratio (D/d)
Side F					
0.50	16.00	0.50	12.00	0.20	15.00
1.00	8.00	1.00	6.00	0.40	7.50
2.00	4.00	1.50	4.00	0.60	5.00
3.00	2.67	2.00	3.00	0.80	3.75
4.00	2.00	2.50	2.40	1.00	3.00
5.00	1.60	3.00	2.00	1.20	2.50
Side R					
5.00	1.60	2.80	2.14	2.00	1.50
4.50	1.78	2.30	2.61	1.80	1.67
3.50	2.29	1.80	3.33	1.60	1.88
2.50	3.20	1.30	4.62	1.40	2.14
1.50	5.33	0.80	7.50	1.20	2.50
0.50	16.00	0.30	20.00	1.00	3.00

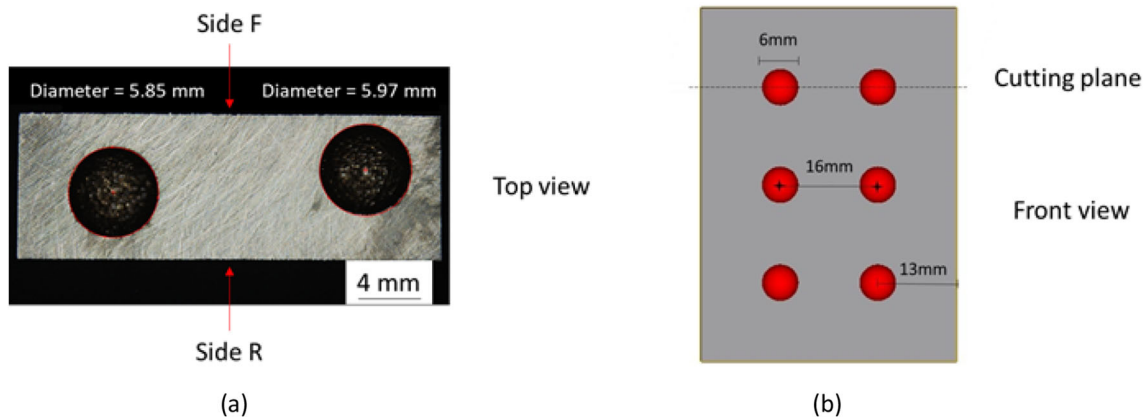


Fig. 6 a Section of specimen 2 after a macrographic analysis related to the spherical defects indicated in (b)

4.2 Setup for Pulsed Tests

The pulsed thermographic tests were performed in reflection configuration using the experimental setup shown in Fig. 7, composed of an MWIR (range 3.0–5.0 μm) cooled sensor FLIR A6751, with a thermal sensitivity/NETD < 18 mK, a full frame window of 640 × 512 pixels and a lens of 50 mm, and two flash lamps (Hensel EH Pro 6000, Fairfield, NJ, USA) with an optical pulse energy of 6 kJ and a pulse duration in the range 3–5 ms. For triggering the thermal excitation with the thermal acquisition, the software IRTA2® by DES (Diagnostic Engineering Solutions Srl) was used. Considering the results shown in [7], it is possible to obtain an estimation of the absorbed energy by the specimens during each test, equal to $Q/\rho c = 0.0015 K \cdot m$. The main technical specifications of

the adopted set-up are reported in Table 4. In particular, the adopted values of frame rate and spatial window were chosen considering both the thermophysical material properties and defect characteristics. About 200 tests were carried out, investigating both sides of each specimen, considering four replications as indicated in Table 3, and a maximum surface extension of about 750 mm², including two defects for each test. A duration of 10 s was considered for each acquisition. As explained in [7], considering one-dimensional models and material thermophysical properties obtained by means of the Parker standard method [32], the duration of the acquisitions was sufficient to reach a theoretical depth of about 5 mm, and then to investigate the depths of all the defects (Table 3).

Table 4 Technical specifications related to the adopted thermographic set-up

Set-up technical specifications						
Energy source Flash Hensel EH Pro 6000	Lamps 2	Pulse duration (ms) 3–5	Nominal energy input (kJ) 6			
MWIR 3–5 μm cooled sensor FLIR A6751 – lens 50 mm,	Frame rate (Hz) 600	Acquisition time (s) 10	Calibration temperature range ($^{\circ}\text{C}$) 10–90 $^{\circ}\text{C}$	Integration time (μs) 595.43	Spatial window (pixels) 320 \times 156	Spatial resolution (mm/pixel) 0.14

5 Data Processing Procedure and Results

To obtain the PoD curves, a comparison among different algorithms and related performance was carried out with the aim to assess the advantages and disadvantages of each one and then the capability of thermography of detecting shallow defects with a spherical shape.

The data analysis requires a series of post-processing steps that need to be explained and specified to understand the quality of the achieved results. The following data procedure specifies also the different steps used to obtain the PoD curves.

- Subtraction of the “cold” frame acquired before starting the flash pulse from the entire thermal sequence, to obtain the delta temperature.
- The application of different post-processing algorithms, and subsequent output, described in the previous section:
- PCT, 4096 frames, about 7 s – sequence of maps of the EOFs as a function of time;
- PPT, 4096 frames – 2 sequences of maps (phase and amplitude) as function of frequency;



Fig. 7 Experimental setup adopted for pulsed thermographic tests: energy source with two flash lamps and MWIR cooled sensor FLIR A6751

- TSR, 4096 frames – 2 sequences of maps of 1st and 2nd derivatives, polynomial degree 5 (determined with preliminary tests) as a function of time;
- Linear regression in a log–log scale – analysis of 31 different intervals, not evenly spaced (every 0.1 s until 0.5 s of cooling down, after every 0.25 s until 7 s or 4096 frames), to obtain, also in this case, 2 sequences of maps related to the Slope Coefficient and the Square Correlation Coefficient R^2 [19, 33] as function of interval time.
- Definition of Regions of Interest (ROIs), with a matrix of 3 \times 3 pixels for each defect and four different matrices of 5 \times 5 pixels for the sound material. This latter has been taken around the defect, considering a variable distance, based on the defect diameter, avoiding edge effects, from a minimum of 40 pixels – $D = 3$ mm to a maximum of 60 pixels – $D = 8$ mm, considering the centre of the defect, as here reported in Fig. 8.
- Calculation of the contrast (C) and normalized contrast (CNR), considering the ROIs previously defined and using the following equations, for each thermal feature and post-processing algorithm.

$$C = MS_D - MS_S \quad CNR = \frac{MS_D - MS_S}{SD_S} \quad (6)$$

where MS_D is the mean value related to the defective ROI, MS_S and SD_S are, respectively, the mean and the standard deviation values of the sound ROI.

- Definition of defect detectability, considering the Normalized Contrast (CNR) for each defect and an appropriate threshold value (Th), to carry out the hit/miss response procedure useful to reconstruct the PoD curves. To choose the appropriate threshold value, several attempts were carried out, analysing all the post-processed data. In particular, three values of the threshold were considered, equal to 1, 2, and 3, and the actual adopted threshold value was chosen as the one above of which the signal contrast produces a “visible” defect, according to an inspection carried out by a qualified operator.

Fig. 8 Thermal features related to the application of PCT algorithm – EOF2; an example of result and identification of sound and defect as main ROIs and relative distance

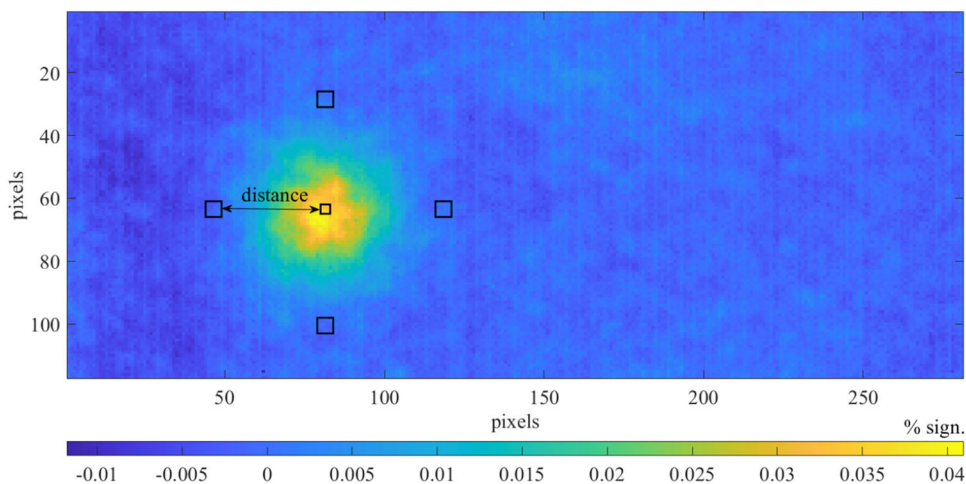
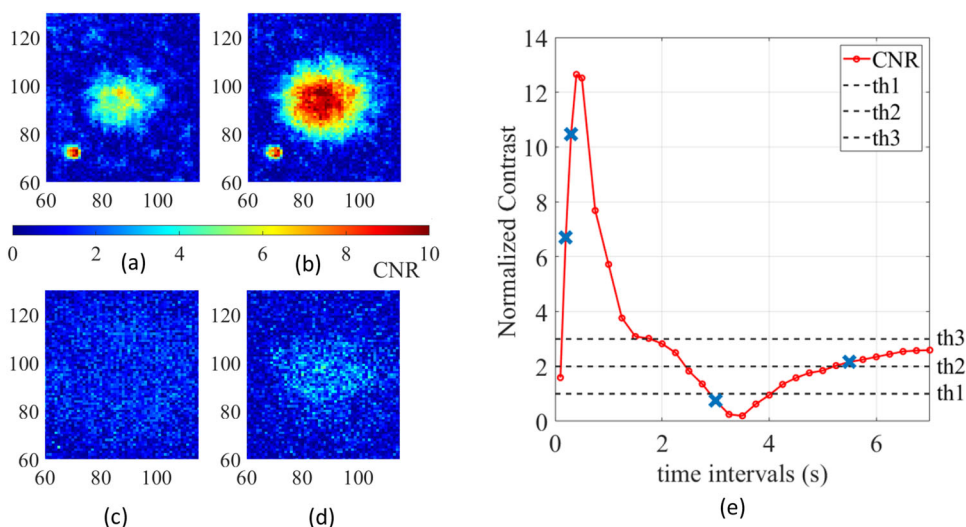


Fig. 9 Definition of the procedure for defect detectability—example of thermal maps related to the slope feature after the CNR calculation pixel by pixel for different intervals of analysis equal to respectively **a** 0.2 s, **b** 0.3 s, **c** 3 s, **d** 5.5 s, and **e** trend related to the normalized contrast (CNR) for all the time intervals; an indication of the different threshold values and times corresponding to the thermal maps is shown on the left (blue crosses)



As an example of the adopted procedure, Figure 9 shows some results related to the larger and more superficial defect, analysing the raw thermal data as previously described and obtaining a sequence of maps for the slope and the R^2 calculated pixel by pixel and considering 31-time intervals, as explained before. The slope results refer to 4 different maps obtained for 4 different time intervals (Figure 9 (a)—0.2 s, 9—0.3 s, 9—3 s and 9—5.5 s). Figure 9e shows the trend of both the contrast and the normalized contrast for all the time intervals. Considering the results in Figure 9, a CNR value greater than 2 seems to correspond to a “visible” detectable defect. Similar results were obtained considering the other algorithms and the other defects and then a threshold value (Th) equal to 2 can be adopted to define the defect detectability as follows:

$$\begin{cases} hit & 1 \quad S_{TF}(x, y) > MS_S + |MS_D - MS_S|Th \\ miss & 0 \quad S_{TF}(x, y) < MS_S + |MS_D - MS_S|Th \end{cases} \quad (7)$$

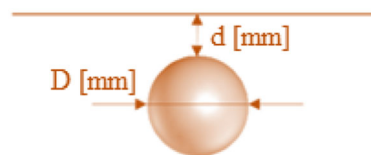


Fig. 10 A simple scheme that defines the response ‘ \hat{a} ’ and so the chosen parameter to represent the defect geometry

Equation 7 represents the conditions for which the generic pixel (x, y) related to the obtained result or thermal feature has a signal value indicated as S_{TF} , which can be assumed equal to 1 or 0 depending on the chosen threshold value (hit/miss data).

- Determination for each output sequence, the map that provides the maximum normalized contrast.
- Definition of the parameter ‘ a ’ that represents the maximum normalized contrast value for each thermal feature.

- Definition of the response that describes the defect geometry ' \hat{a} ', equal to the defect aspect ratio D/d (defined in Fig. 10).
- Comparing four possible models ' \hat{a} vs. a ', ' \hat{a} vs. $\log(a)$ ', ' $\log(\hat{a})$ vs. a ', and ' $\log(\hat{a})$ vs. $\log(a)$ ', and choosing the best one that returns the greater R^2 – linearity value, together with a low norm of the residual. This analysis has been carried out for all the implemented algorithms and thermal features. From the graphic results reported as an example in Fig. 11, it was possible to conclude that the source data of “ CNR vs. D/d ” presents the most linear correlation (different colours were used based on the defect diameter value).
- For all the algorithms and investigated thermal features, the slope, and intercept values were obtained considering the linear model “ CNR vs. D/d ” and then the goodness of linear fitting has been evaluated considering 95% confidence and prediction bounds, as shown in the example reported below in the case of PCT analysis.

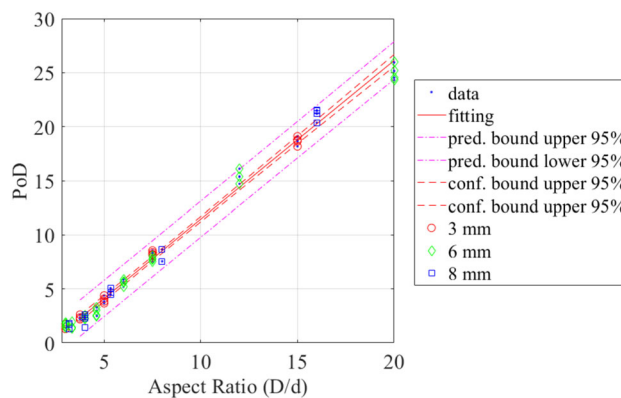


Fig. 12 A linear relationship between the maximum normalized contrast and the defect aspect ratio D/d , considering the PCT results – linear fit, confidence, and prediction bounds

- In all the cases, the log-odds model was used to plot the PoD curves. Furthermore, for each data processing

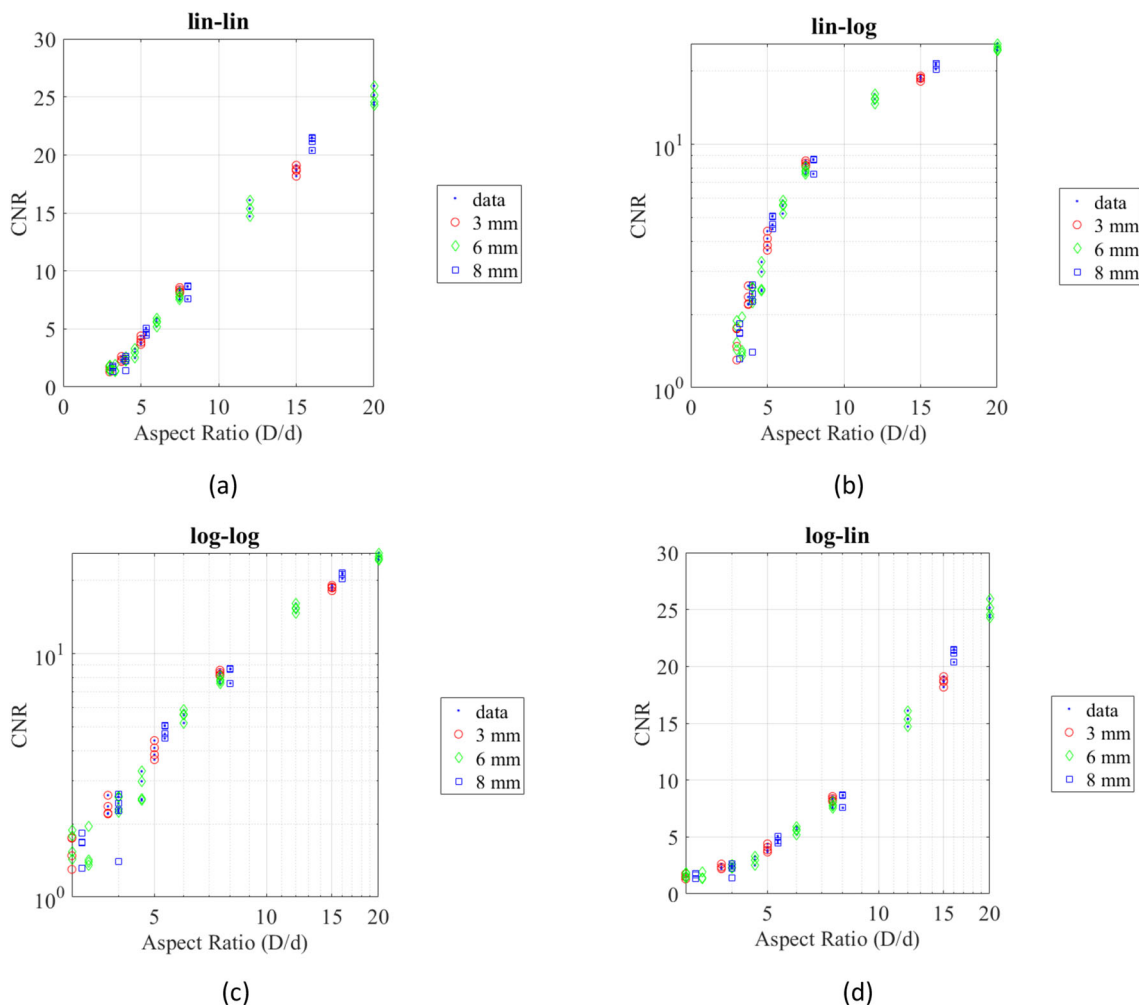


Fig. 11 Four models comparison in the case of PCT results, considering all the defects, the replications and the result related to the maximum CNR vs defect aspect ratio D/d ; **a** lin-lin, **b** lin-log, **c** log-log, **d** log-lin

- method, the 95% lower confidence bounds were also calculated and reported.
- Comparison of the obtained results in terms of PoD curves considering the defect aspect ratio with 90% PoD (D/d_{90}) and the defect aspect ratio for which a 90% PoD is reached at 95% confidence level ($D/d_{90/95}$), for each thermal feature and post-processing analysis

6 Comparison Among Algorithms and Discussion

Following the different steps indicated before, all the acquired thermal sequences were analysed, obtaining, as a result, the associated PoD curves. As already specified, the maximum contrast related to the trend of each thermal feature was considered and associated with the related defect aspect ratio. In Fig. 13 are resumed all the obtained results in terms of PoD curves, for each algorithm, as already shown in the case of PCT in Fig. 14, using the log-odds model. The lower and upper confidence and prediction bounds at 95% were calculated and reported in each graph.

In Fig. 15, the comparison among the different algorithms is shown within the same graph, leaving, for simplicity and clarity of results, only the curves related to the lower confidence bound at 95%. The number of the detected defects and the coefficient R^2 are also indicated for each algorithm and thermal feature.

A zoom of the higher part of the PoD curves are reported in Fig. 16 and then in Table 5. For clarity, in Fig. 15, different symbols have been assigned to each PoD curve for a simpler and more immediate distinction. In particular, for each algorithm two different results can be obtained: the values of the defect aspect ratio associated with a PoD of 90% (D/d_{90}) and the ones with a 90% probability where only 5% might fall outside the confidence limit in case the experiment is repeated

four (AM process + thermographic measurements and analysis) times ($D/d_{90/95}$). The indication $D/d_{90/95}$, together with the linearity (R^2), represents a measure to quantify the differences between the fit curve and experimental data for each algorithm. Within the same table, the detection rate with respect to the total number of inspected defects (144) is also indicated.

As already demonstrated in previous works for other applications and case studies [19], the post-processing algorithms show intrinsic peculiarities and limitations. From the analysis of Table 5 and Fig. 15, the higher D/d values, and so the worst results, are related to PCT and R^2 algorithms while, the best results are obtained with the TSR algorithm, with the lowest D/d values. However, considering the results reported in Table 5 related to the number of detected defects and the detection rate, the PCT algorithm shows better results if compared with Slope, R^2 and PPT, but with a lower probability of detection.

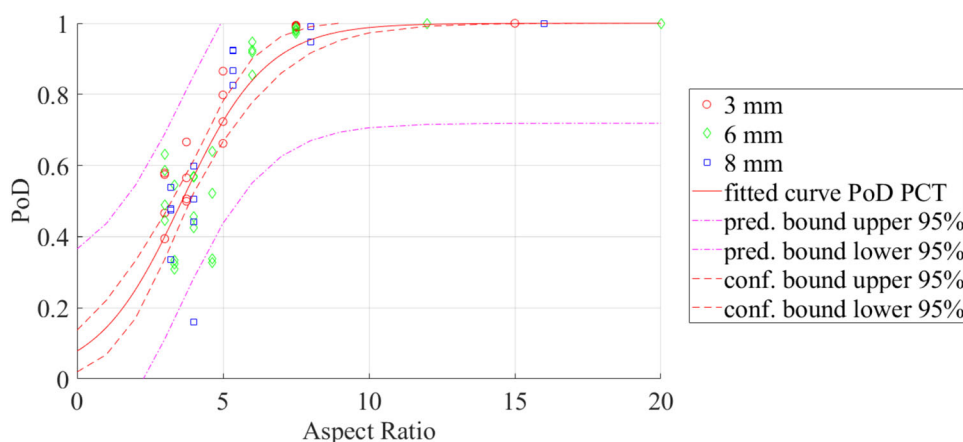
To have an idea of the limits of each algorithm and thermal features, not only related to defect aspect ratio D/d , but also considering the single values in terms of diameter and depth, the results in terms of normalized contrast CNR are reported in a 3D plot (Fig. 17), setting directly in the graphs the CNR limit equal to 2. The representation regards the detected spherical defects, reporting the single data of each replication.

As already demonstrated in [26], the signal contrast, is most affected by the depth with respect to the defect size, i.e. the contrast decreases with the squared depth (Eq. 1), while it seems to show a linear dependence with the in-plane defect dimension.

Also, the graphs in Fig. 17, show the limits of the technique in terms of depth, with a maximum value of 2 mm in correspondence of a diameter equal to 6 mm, in the case of the TSR algorithm.

In Table 6, the previous results are summarized, indicating for each diameter the maximum detectable depth and the corresponding aspect ratio D/d value. These values refer to

Fig. 13 PoD curves for different algorithms and analysed thermal features—log-odds model; **a** slope, **b** R^2 , **c** amplitude, **d** phase, **e** TSR 1der, **f** TSR 2der (see Fig. 12 for PCT)



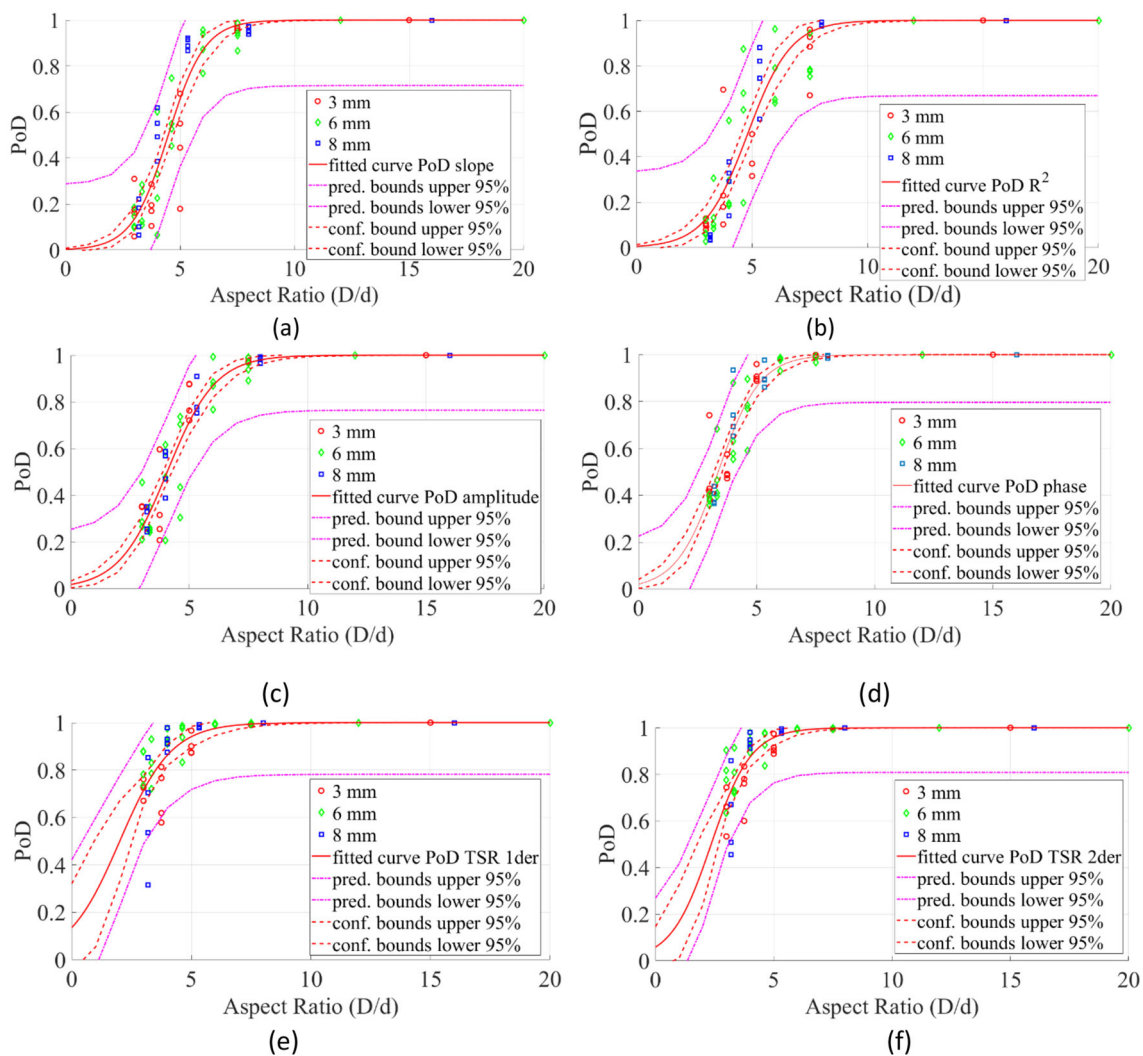


Fig. 14 POD curve—log-odds model; example related to the PCT result

Fig. 15 Comparison among PoD curves for different algorithms and analysed thermal features

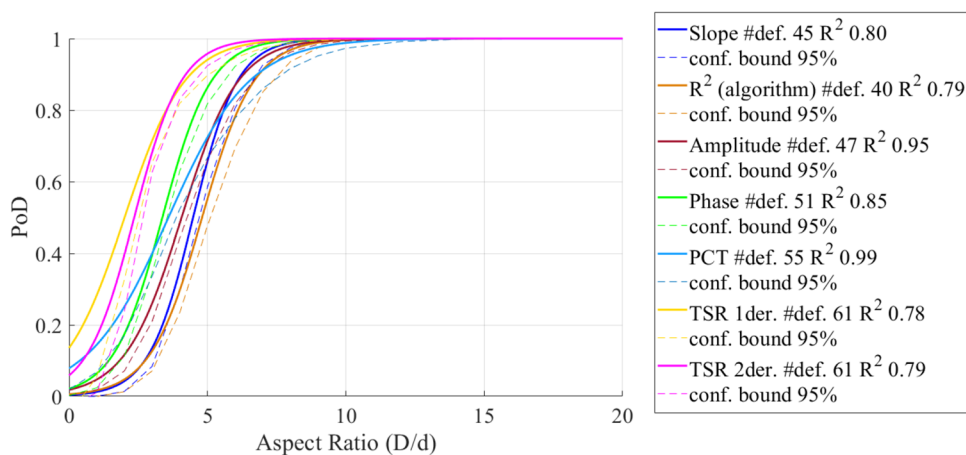


Fig. 16 A zoom of PoD curves for different algorithms and analysed thermal features to highlight the PoD 90% and the PoD 90/95%

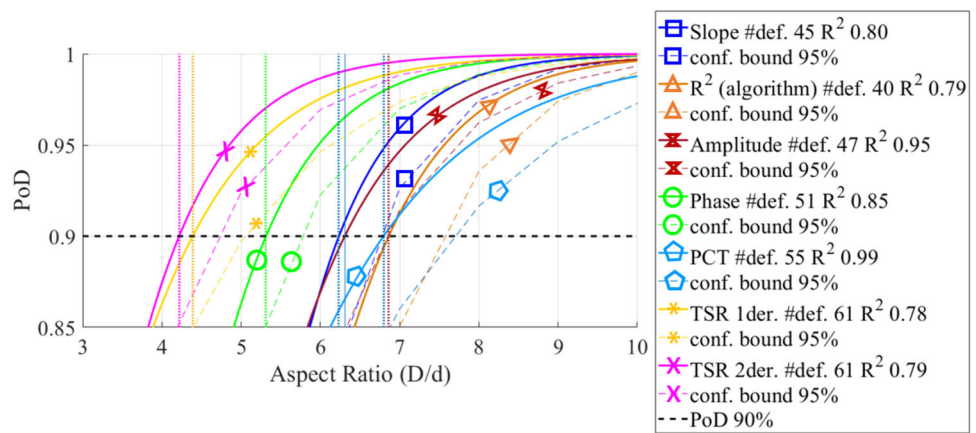


Table 5 D/d_{90} and $D/d_{90/95}$ values obtained using different data processing algorithms and thermal features on hit/miss data and a summary of detection results in terms of the number of detected defects and detection rate

Algorithms	$D/d_{90/95}$	D/d_{90}	Number of detected defects	Detection rate (%)
Slope	6.8	6.2	45	31
R^2	7.6	6.9	40	28
Amplitude	6.9	6.3	47	33
Phase	5.8	5.3	51	35
PCT	7.7	6.8	55	38
TSR 1der	5.0	4.4	61	42
TSR 2der	4.7	4.2	61	42

an imposed defect, for the continuous values it is necessary to refer to the proposed PoD curves. As demonstrated also in previous works [19], PCT presents the best results in terms of CNR (Fig. 17).

Therefore, the limit of the pulsed technique associated with the adopted flash setup generally rises to a D/d value equal to 3 in the case of spherical defects, with a probability of detection that is around 70% with the TSR algorithm.

7 Conclusions

A complete study regarding the probability of detection for spherical shallow defects by means of Pulsed Thermography has been proposed. Different specimens in AISI 316L were produced by means of the L-PBF technology, with shallow spherical defects of different sizes and depths. The main aim was to investigate the capability of this non-destructive technique of detecting defects with geometry very different from the FBHs, usually used for metallic materials (high diffusive materials).

As quantitative analysis, the PoD methodology has been adopted to define the limits and advantages of this technique applicated as offline control. Two flash lamps and a cooled sensor were adopted, and different post-processing algorithms were adoptes for extracting the thermal features from the thermal sequences to characterize these defects. As

the main parameters to quantify the detected defects, the contrast and then the normalized contrast were chosen. For the defect geometry, the aspect ratio D/d was defined, being D the maximum diameter of the sphere and d the depth of the sphere from its starting point with respect to the specimen surface.

The main results can be summarized by the following points:

- Considering the adopted setup, approach and procedure for data analysis, Pulsed Thermography presents a $\geq 50\%$ probability of detecting spherical defects with $D/d > 4$, independently from the used algorithm.
- For higher values of D/d ($D/d > 6.5$), the probability of detecting the defect rises to 90% or higher, based on the used algorithm.
- For lower values of D/d ($3 < D/d < 4$), the TSR and PCT algorithms allow to detect defects with greater probability, and in particular, the TSR algorithm gives a probability of around 70%.
- Considering the detected defects, the highest depth value is 2 mm, with a diameter equal to 6 mm, using the TSR algorithm.
- Spherical defects, closer to real defects such as porosity, can be detected in correspondence of a minimum aspect ratio of 3–4, higher than the limit usually obtained with Flat Bottom Hole (FBH).

Finally, as expected, shallow spherical defects are more difficult to detect with respect to FBHs and in this regard, they provide a more realistic indication of the capability of AT of detecting real defects such as isolated porosities. It is worth noting that the obtained results are related to not only simple empty spheres but spheres with powder inside of the same material. These kinds of defects, even if of smaller sizes, can occur during the process due to undesired changes of some process parameters and provide a reduced signal contrast with respect to porosity with air inside.

As an example, looking at the obtained results in terms of PoD curves, porosities with the size of about 1 mm (typical of processes for obtaining metal alloys) could be detected with a probability of detection of about 70% inspecting the sub-surface deposition layers, with depths around 0.2 or 0.3 mm.

It is important to underline that, in this work, the limits of the PT technique are related to the equipment used for the tests and probably can be improved by using high-power heat sources or/and more performing IR sensors. As already suggested in previous works and here remarked, the thermography inspection can be also used for off-line control AM components. Of course, it is worth underlining that the capability of the AT technique is confined only within the inspection of the shallow defects.

Fig. 17 3D plots related to each algorithm and adopted thermal feature; **a** slope, **b** R^2 , **c** amplitude, **d** phase, **e** PCT, **f** TSR 1der., **g** TSR 2der

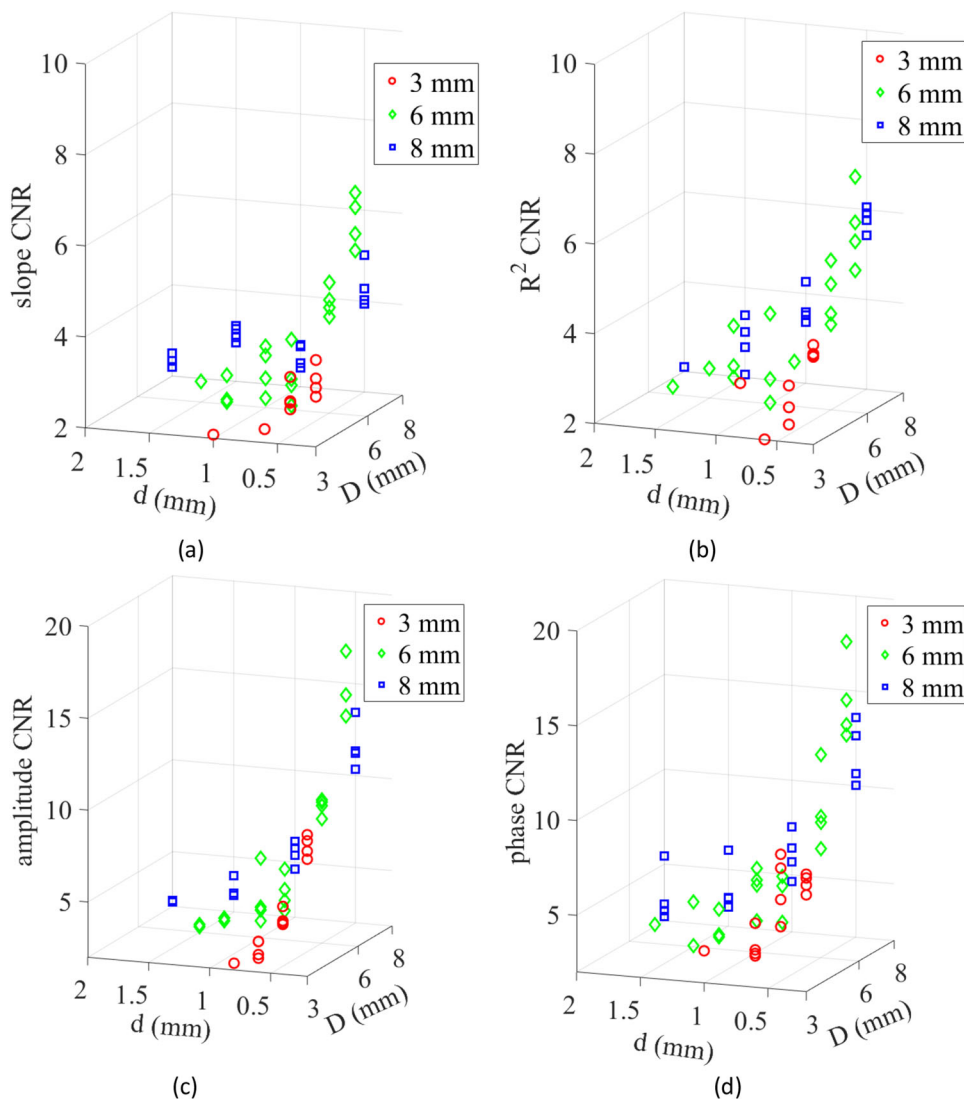


Fig. 17 continued

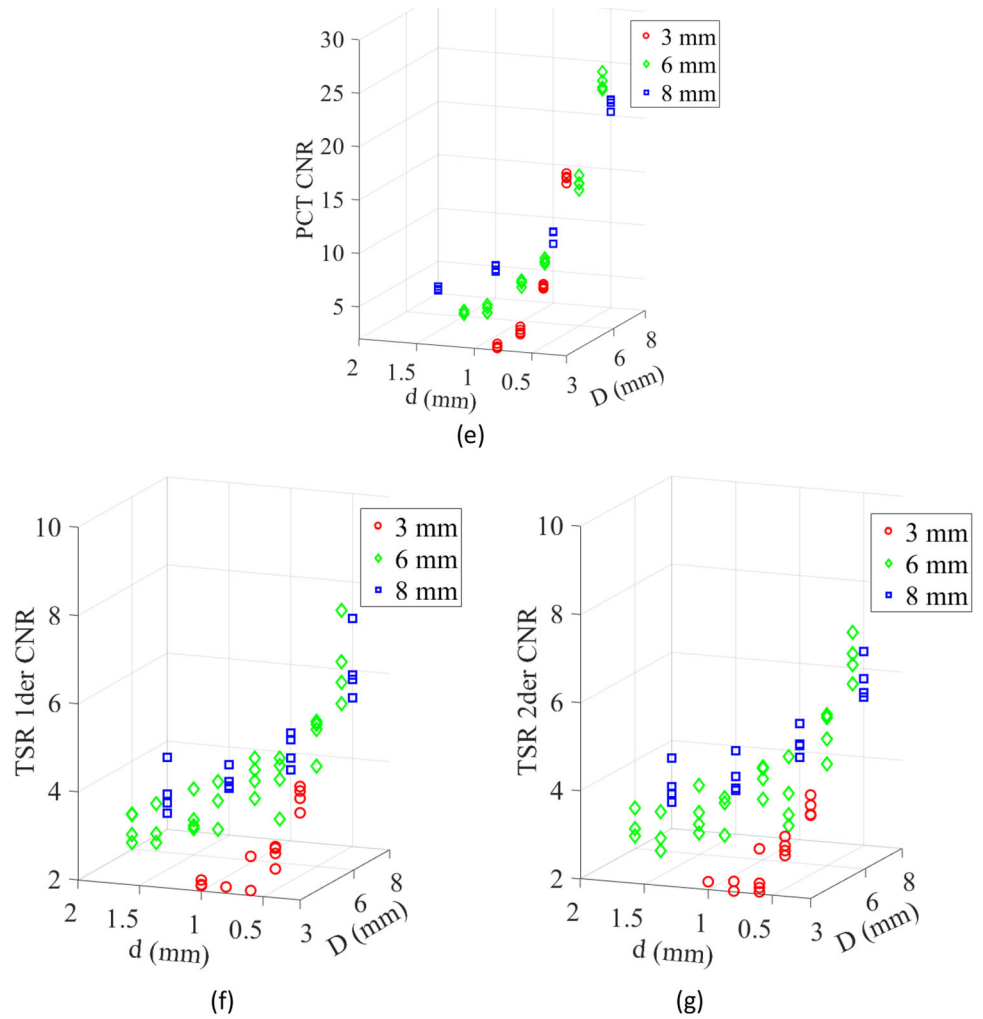


Table 6 Summary of the detected defects considering the depth and 2D dimension separately

Thermal feature or post-processing algorithm	D (mm)	d_{max} (mm)	D/d	Thermal feature	D (mm)	d_{max} (mm)	D/d
Slope	3	1	3	R^2	3	0.8	3.75
	6	1.5	4		6	1.8	3.33
	8	2	4		8	2	4
Amplitude	3	0.8	3.75	Phase	3	1	3
	6	1.5	4		6	1.8	3.33
	8	2	4		8	2	4
PCT	3	0.8	3.75				
	6	1.5	4				
	8	2	4				
TSR 1der	3	1	3	TSR 2der	3	1	3
	6	2	3		6	2	3
	8	2	4		8	2	4

Acknowledgements The authors want to thank Ing. Giuseppe Danilo Addante for the work carried out during his master's degree thesis, which focused on data analysis for some algorithms discussed and presented in this work; furthermore the authors want to thank Prof. Sabina Luisa Campanelli for her valuable contribution and support in the research.

Author Contributions Conceptualization - ED'A, Methodology - ED'A, DP, Validation - ED'A, DP, AA, VE, AF, Formal analysis - ED'A, Investigation - ED'A, DP, VE, AF, Resources - UG, AA, Data Curation - ED'A, Writing Original Draft - ED'A, VE, Writing, Review and Editing - ED'A, DP, VE, AA, Supervision - UG, AA, DP. All authors reviewed and approved the manuscript for final submission.

Funding Open access funding provided by Politecnico di Bari within the CRUI-CARE Agreement. This work is founded by the project Dipartimento di Eccellenza—Dipartimento di Meccanica, Matematica e Management (DMMM) del Politecnico di Bari—post doc research grant—topic and title of the assigned research “Development of innovative techniques for structural integrity control and mechanical characterization of components obtained with innovative technological processes”.

Data Availability The data presented in this study are available on request from the first author.

Declarations

Conflict of interest The authors declare no conflict of interest. The funders had no role in the design of the study; in the collection, analyses, or interpretation of data; in the writing of the manuscript, or in the decision to publish the results.

Open Access This article is licensed under a Creative Commons Attribution 4.0 International License, which permits use, sharing, adaptation, distribution and reproduction in any medium or format, as long as you give appropriate credit to the original author(s) and the source, provide a link to the Creative Commons licence, and indicate if changes were made. The images or other third party material in this article are included in the article's Creative Commons licence, unless indicated otherwise in a credit line to the material. If material is not included in the article's Creative Commons licence and your intended use is not permitted by statutory regulation or exceeds the permitted use, you will need to obtain permission directly from the copyright holder. To view a copy of this licence, visit <http://creativecommons.org/licenses/by/4.0/>.

References

- Maldague, X. (2001). Theory and practice of infrared technology for nondestructive testing.
- Duan, Y., Servais, P., Genest, M., Ibarra-Castanedo, C., Maldague, X.P.: ThermoPoD: A reliability study on active infrared thermography for the inspection of composite materials. *J. Mech. Sci. Technol.* **26**(7), 1985–1991 (2012)
- Rothbart, N., Maierhofer, C., Goldammer, M., Hohlstein, F., Koch, J., Kryukov, I., Sengebusch, M.: Probability of detection analysis of round robin test results performed by flash thermography. *Quant. InfraRed Thermogr. J.* **14**(1), 1–23 (2017)
- Meola, C., Boccardi, S., Carlomagno, G.M. (eds.): *Infrared thermography in the evaluation of aerospace composite materials: infrared thermography to composites*. Woodhead Publishing, Sawston (2016)
- D'Accardi, E., Dell'Avvocato, G., Palumbo, D., & Galietti, U. (2021, April). Limits and advantages in using low-cost microbolometric IR-camera in lock-in thermography for CFRP applications. In *Thermosense: Thermal Infrared Applications XLIII* (Vol. 11743, p. 117430L). International Society for Optics and Photonics.
- Ibarra-Castanedo, C., Avdelidis, N. P., & Maldague, X. P. (2005, March). Quantitative pulsed phase thermography applied to steel plates. In *Thermosense XXVII* (Vol. 5782, pp. 342–351). International Society for Optics and Photonics.
- D'Accardi, E., Krankenhagen, R., Ulbricht, A., Pelkner, M., Pohl, R., Palumbo, D., & Galietti, U. (2022). Capability to detect and localize typical defects of laser powder bed fusion (L-PBF) process: an experimental investigation with different non-destructive techniques. *Progress in Additive Manufacturing*, 1–18.
- D'Accardi, E., Palumbo, D., Errico, V., Fusco, A., & Galietti, U. (2022). A first quantitative approach for detecting volumetric defects in additive manufactured metal samples by using active thermographic technique. In *IOP Conference Series: Materials Science and Engineering* (Vol. 1214, No. 1, p. 012015). IOP Publishing.
- Chulkov, A.O., Tuschl, C., Nesteruk, D.A., Oswald-Tranta, B., Vavilov, V.P., Kuimova, M.V.: The detection and characterization of defects in metal/non-metal sandwich structures by thermal NDT, and a comparison of areal heating and scanned linear heating by optical and inductive methods. *J. Nondestr. Eval.* **40**(2), 1–13 (2021)
- Ahmad, J., Akula, A., Mulaveesala, R., Sardana, H.K.: Probability of detecting the deep defects in steel sample using frequency modulated independent component thermography. *IEEE Sens. J.* **21**(10), 11244–11252 (2020)
- Wei, Y., Ye, Y., He, H., Su, Z., Ding, L., Zhang, D.: Multi-frequency fused lock-in thermography in detecting defects at different depths. *J. Nondestr. Eval.* **41**(3), 1–10 (2022)
- Hirsch, P., Malekmohammadi, H., Ahmadi, S., Hassenstein, C., Pech-May, N. W., Laureti, S., Ziegler, M. Temporal shaping and pulse-compression in thermography using laser heating.
- Geng, C., Shi, W., Liu, Z., Xie, H., He, W.: Nondestructive surface crack detection of laser-repaired components by laser scanning thermography. *Appl. Sci.* **12**(11), 5665 (2022)
- Silipigni, G., Burrascano, P., Hutchins, D.A., Laureti, S., Petrucci, R., Senni, L., Ricci, M.: Optimization of the pulse-compression technique applied to the infrared thermography nondestructive evaluation. *NDT & E Int.* **87**, 100–110 (2017)
- Ibarra-Castanedo, C., Bendada, A. and Maldague, X. (2005). Image and signal processing techniques in pulsed thermography. *GESTS Int'l Trans. Computer Science and Engr.*, 22(1): 89–100.
- Shepard, S. M. (2001). *Advances in Pulsed Thermography*. Proc. SPIE - The International Society for Optical Engineering, Thermosense XXVIII, Orlando, FL, 2001, Eds. A. E. Rozlosnik and R. B. Dinwiddie, 4360:511–515.
- Roche, J.M., Passilly, F., Balageas, D.: A TSR-based quantitative processing procedure to synthesize thermal D-scans of real-life damage in composite structures. *J. Nondestr. Eval.* **34**(4), 1–15 (2015)
- Rajic, N. *Principal Component Thermography*. (2002) DEFENCE SCIENCE & TECHNOLOGY, Airframes and Engines Division Aeronautical and Maritime Research Laboratory, DSTO-TR-1298.
- D'Accardi, E., Palumbo, D., Tamborrino, R., Galietti, U.: A quantitative comparison among different algorithms for defects detection on aluminum with the pulsed thermography technique. *Metals* **8**(10), 859 (2018)
- Montinaro, N., Cerniglia, D., Pitarresi, G.: A numerical and experimental study through laser thermography for defect detection on

- metal additive manufactured parts. *Frattura ed Integrità Strutturale* **12**(43), 231–240 (2018)
21. Pavlovic, M., Takahashi, K., Müller, C., et al. Reliability in non-destructive testing (NDT) of the canister components. NDT Reliability – Final Report. SKB Technical report R-08-129, ISSN 1402-3091, Swedish Nuclear Fuel and Waste Management Co.; 2008. Available from: http://www.iaea.org/inis/collection/NCICollectionStore/_Public/40/057/40057523.pdf.
 22. Nondestructive evaluation System Reliability Assessment. Department of Defense Handbook MII-HDBK-1823. AMSC N/A AReA NDTI; 1999. Available from: [http://www.statisticalengineering.com/mh1823/MIH-HDBK-1823A\(2009\).pdf](http://www.statisticalengineering.com/mh1823/MIH-HDBK-1823A(2009).pdf).
 23. Müller, C., Bertovic, M., Pavlovic, M., et al. Holistically evaluating the reliability of NDe systems –paradigm shift. In: Proceedings of the 18th World Conference on Nondestructive Testing; 2012 April 16–20; Durban, South Africa; 2012. Available from: http://www.ndt.net/search/link.php?id=12498&file=article/wcndt2012/papers/591_wcndtfinal00590.pdf.
 24. Kurz, J.H., Jüngert, A., Dugan, S., Dobmann, G., Boller, C.: Reliability considerations of NDT by probability of detection (POD) determination using ultrasound phased array. *Eng. Fail. Anal.* **35**, 609–617 (2013)
 25. Matzkanin, G. A., & Yolken, H. T. (2001). *Probability of detection (POD) for Nondestructive Evaluation (NDE)*. NONDESTRUCTIVE TESTING INFORMATION ANALYSIS CENTER AUSTIN TX.
 26. Angioni, S.L., Ciampa, F., Pinto, F., Scarselli, G., Almond, D.P., Meo, M.: An analytical model for defect depth estimation using pulsed thermography. *Exp. Mech.* **56**(6), 1111–1122 (2016)
 27. Moskovchenko, A.I., Švantner, M., Vavilov, V.P., Chulkov, A.O.: Characterizing depth of defects with low size/depth aspect ratio and low thermal reflection by using pulsed IR thermography. *Materials* **14**(8), 1886 (2021)
 28. Errico, V., Fusco, A., Campanelli, S.L.: Effect of DED coating and DED + Laser scanning on surface performance of L-PBF stainless steel parts. *Surf. Coatings Technol.* **429**, 127965 (2022). <https://doi.org/10.1016/j.surfcoat.2021.127965>
 29. Campanelli, S.L., Contuzzi, N., Posa, P., Angelastro, A.: Study of the aging treatment on selective laser melted maraging 300 steel. *Mater Res Express* **6**, 66580 (2019). <https://doi.org/10.1088/2053-1591/ab0c6e>
 30. Lu, Y., Wu, S., Gan, Y., et al.: Study on the microstructure, mechanical property and residual stress of SLM Inconel-718 alloy manufactured by differing island scanning strategy. *Opt Laser Technol* **75**, 197–206 (2015). <https://doi.org/10.1016/j.optlastec.2015.07.009>
 31. Angelastro, A., Campanelli, S.L.: An integrated analytical model for the forecasting of the molten pool dimensions in Selective Laser Melting. *Laser Phys.* (2022). <https://doi.org/10.1088/1555-6611/ac4098>
 32. ASTM Standard: E1461–13 Standard Test Method for Thermal Diffusivity by the Flash Method. ASTM International, West Conshohocken (2013)
 33. Dell’Avvocato, G., Gohlke, D., Palumbo, D., Krankenhagen, R., Galiotti, U. (2022, May). Quantitative evaluation of the welded area in Resistance Projection Welded (RPW) thin joints by pulsed laser thermography. In *Thermosense: Thermal Infrared Applications XLIV* (Vol. 12109, pp. 152–165). SPIE

Publisher’s Note Springer Nature remains neutral with regard to jurisdictional claims in published maps and institutional affiliations.